

PSFC/JA-00-5

**Electron Beam Halo Formation in High-Power  
Periodic Permanent Magnet Focusing  
Klystron Amplifiers**

R. Pakter and C. Chen

February, 2000

Plasma Science and Fusion Center  
Massachusetts Institute of Technology  
Cambridge, MA 02139, USA

This work was supported by the Air Force Office of Scientific Research, Grant No. F49620-97-1-0325, and in part by the Department of Energy, Office of High Energy and Nuclear Physics, Grant No. DE-FG02-95ER-40919. Reproduction, translation, publication, use and disposal, in whole or part, by or for the United States government is permitted.

To appear in IEEE Transaction on Plasma Science Eighth Special Issue on High-Power Microwave Generation, June (2000).

# **ELECTRON BEAM HALO FORMATION IN HIGH-POWER PERIODIC PERMANENT MAGNET FOCUSING KLYSTRON AMPLIFIERS**

R. Pakter and C. Chen

Plasma Science and Fusion Center  
Massachusetts Institute of Technology  
Cambridge, Massachusetts 02139

## **ABSTRACT**

Electron beam halo formation is studied as a potential mechanism for electron beam losses in high-power periodic permanent magnet focusing klystron amplifiers. In particular, a two-dimensional self-consistent electrostatic model is used to analyze equilibrium beam transport in a periodic magnetic focusing field in the absence of radio-frequency signal, and the behavior of a high-intensity electron beam under a current-oscillation-induced mismatch between the beam and the periodic magnetic focusing field. Detailed simulation results are presented for choices of system parameters corresponding to the 50 MW, 11.4 GHz periodic permanent magnet (PPM) focusing klystron experiment performed at the Stanford Linear Accelerator Center (SLAC). It is found from the self-consistent simulations that sizable halos appear after the beam envelope undergoes several oscillations, and that the residual magnetic field at the cathode plays an important role in delaying the halo formation process.

Keywords: halo formation, klystron, periodic permanent magnet focusing, and microwave source.

## I. INTRODUCTION

One of the main thrusts in high-power microwave (HPM) research is to overcome the problem of radio-frequency (RF) pulse shortening [1,2]. Several mechanisms of RF pulse shortening have been proposed [3], ranging from plasma formation at various locations in the device to nonlinear effects at the RF output section [4-7]. However, few of them have been fully verified in terms of theory, simulation and experiment. In this paper, we discuss halos around high-intensity electron beams as a mechanism by which electron beam loss and subsequent plasma formation may occur in high-power klystron amplifiers.

From the point of view of beam transport in a periodic or uniform solenoidal focusing field, there are two main processes for halo formation in high-intensity electron beams. One process is caused by a mismatch in the root-mean-square (rms) beam envelope [8], and the other is due to a mismatch in the electron phase-space distribution [9]. Both processes can occur when the beam intensity is sufficiently high so that the electron beam becomes space-charge-dominated. The purpose of this paper is to show that the former is responsible for electron beam halos in high-power klystron amplifiers.

For a periodic solenoidal focusing channel with periodicity length  $S$  and vacuum phase advance  $\sigma_0$ , a *space-charge-dominated electron beam* satisfies the condition [8]

$$\frac{SK}{4\sigma_0\varepsilon} = 2.9 \times 10^{-5} \frac{1}{\sigma_0} \left( \frac{S}{\varepsilon_n} \right) \frac{I_b}{\gamma_b^2 \beta_b^2} > 1,$$

(1)

where  $K = 2e^2 N_b / \gamma_b^3 \beta_b^2 m c^2$  is the normalized self-field perveance,  $I_b$  is the electron beam current in amperes,  $\varepsilon_n = \gamma_b \beta_b \varepsilon$  is the normalized rms emittance in meter-radians, and  $S$  is in meters. In the expressions for the self-field perveance  $K$  and the normalized rms emittance  $\varepsilon_n$ ,  $N_b$  is the number of electrons per unit axial length,  $m$  and  $-e$  are the electron rest mass and charge, respectively,  $c$  is the speed of light in *vacuo*, and  $\gamma_b = (1 - \beta_b^2)^{-1/2}$  is the characteristic relativistic mass factor for the electrons. The emittance is essentially the beam radius times a measure of randomness in the transverse electron motion. For a uniform density beam with radius  $a$  and temperature  $T_b$ , the normalized rms emittance  $\varepsilon_n$  is given by

$$\varepsilon_n = \gamma_b \beta_b \varepsilon = \frac{a}{2} \left( \frac{\gamma_b k_B T_b}{mc^2} \right)^{1/2}, \quad (2)$$

where  $k_B$  is the Boltzmann constant.

In particular, we study equilibrium beam transport in a periodic magnetic focusing field in the absence of RF signal and the behavior of a high-intensity electron beam under a current-oscillation-induced mismatch between the beam and the periodic magnetic focusing field, using a two-dimensional self-consistent electrostatic model. Detailed simulation results are presented for choices of system parameters corresponding to the 50 MW, 11.4 GHz periodic permanent magnet (PPM) focusing klystron experiment [10] performed at the Stanford Linear Accelerator Center (SLAC). It is found from the self-consistent simulations that sizable halos appear after the beam envelope undergoes several oscillations, and that the residual magnetic field at the cathode plays an important role in delaying the halo formation process.

The paper is organized as follows. In Section II, a two-dimensional self-consistent model is presented for transverse electrostatic interactions in a high-intensity relativistic electron beam propagating in a periodic focusing magnetic field. In Section III, the equilibrium state for intense electron beam propagation through a PPM focusing field is discussed, the equilibrium (well-matched) beam envelope is determined, and self-consistent simulations of equilibrium beam transport are performed. In Section IV, the effects of large-amplitude charge-density and current oscillations on inducing mismatched beam envelope oscillations are discussed, and use is made of the model presented in Section II to study the process of halo formation in a high-intensity electron beam. The results are compared with the SLAC PPM focusing klystron amplifier experiment. In Section V, conclusions are given.

## II. MODEL AND ASSUMPTIONS

We consider a high-intensity relativistic electron beam propagating with axial velocity  $\beta_b c \hat{e}_z$  through the periodic focusing magnetic field

$$\vec{B}^{ext}(x, y, s) = B_z(s) \hat{e}_z - \frac{1}{2} B'_z(s) (x \hat{e}_x + y \hat{e}_y), \quad (3)$$

where  $s = z$  is the axial coordinate,  $x\hat{e}_x + y\hat{e}_y$  is the transverse displacement from the  $z$ -axis,  $B_z(s+S) = B_z(s)$ ,  $S$  is the fundamental periodicity length of the focusing field, and the prime denotes derivative with respect to  $s$ .

In the present two-dimensional analysis, we treat only the transverse electrostatic interactions in the electron beam. The effects of longitudinal charge-density and current oscillations in the electron beam, which are treated using the relativistic Lorentz equation and full Maxwell equations, will be considered in Section IV. For present purposes, we make the usual thin-beam approximation, assuming that (a) the Budker parameter is small, i.e.,  $e^2 N_b / \gamma_b m c^2 \ll 1$ , (b) the beam is thin compared with the lattice period  $S$ , and (c) the electron motion in the transverse direction is nonrelativistic.

Under the thin beam approximation, the self-consistent electrostatic interactions in the electron beam can be described by a two-dimensional model involving  $N_p$  macroparticles (i.e., charged rods). In the Larmor frame, the transverse dynamics of the macroparticles is governed by [8,11]

$$\frac{d^2 x_i}{ds^2} + \kappa_z(s) x_i - \frac{e}{\gamma_b^3 \beta_b^2 m c^2} \frac{\partial}{\partial x_i} \phi^s(x_i, y_i, s) = 0, \quad (4)$$

$$\frac{d^2 y_i}{ds^2} + \kappa_z(s) y_i - \frac{e}{\gamma_b^3 \beta_b^2 m c^2} \frac{\partial}{\partial y_i} \phi^s(x_i, y_i, s) = 0, \quad (5)$$

where  $i = 1, 2, \dots, N_p$ , and the focusing parameter  $\kappa_z(s)$  and self-field potential  $\phi^s(x_i, y_i, s)$  are defined by

$$\kappa_z(s) = \left[ \frac{e B_z(s)}{2 \gamma_b \beta_b m c^2} \right]^2 = \left[ \frac{\Omega_c(s)}{2 \beta_b c} \right]^2, \quad (6)$$

$$\mathbf{f}^s(x_i, y_i, s) = - \frac{e N_b}{N_p} \sum_{j=1(j \neq i)}^{N_p} \ln \left\{ \frac{[x_i - x_j]^2 + [y_i - y_j]^2}{[x_i - x_j r_w^2 / r_j^2]^2 + [y_i - y_j r_w^2 / r_j^2]^2} \right\}, \quad (7)$$

respectively. Here,  $\Omega_c(s)$  is the (local) relativistic cyclotron frequency associated with the axial magnetic field  $B_z(s)$ , and  $r_i \equiv (x_i^2 + y_i^2)^{1/2}$ . The beam is assumed to propagate inside a perfectly conducting cylindrical tube of radius  $r_w$ , such that the self-field potential satisfies the boundary condition  $\mathbf{f}^s(r_i = r_w, s) = 0$ . Detailed derivations of Eqs. (4)-(7) can be found in [8] for  $r_w \rightarrow \infty$ .

The two-dimensional self-consistent model described by Eqs. (4) and (5) will be used to simulate equilibrium beam transport in a PPM focusing field in the absence of RF signal (Section III) and electron beam halo formation in the transverse direction induced by large-amplitude longitudinal current oscillations (Section IV).

### III. EQUILIBRIUM BEAM TRANSPORT

In the absence of RF signal, the relativistic electron beam propagates through the focusing field in an equilibrium state. In this section, we discuss important properties of the equilibrium beam transport, and present results of our analysis and self-consistent simulations of periodically focused intense electron beam equilibria for choices of system parameters corresponding to those used in the SLAC 50 MW, 11.4 GHz PPM focusing klystron experiment [10].

#### A. Beam Envelope Equation for a Rigid-Rotor Vlasov Equilibrium

It has been shown previously [12,13] that one of the equilibrium states for the system described by Eqs. (4) and (5) is a rigid rotor Vlasov equilibrium in which the beam density is uniform transverse to the direction of beam propagation. The outermost beam radius  $r_b(s) = r_b(s + S)$  obeys the envelope equation [12]

$$\frac{d^2 r_b}{ds^2} + \kappa_z(s) r_b - \frac{K}{r_b} - \frac{\langle \hat{P}_\theta \rangle^2}{r_b^3} - \frac{(4\varepsilon)^2}{r_b^3} = 0, \quad (8)$$

where  $\gamma_b \beta_b m c \langle \hat{P}_\theta \rangle = \text{constant}$  is the macroscopic canonical angular momentum of the beam at  $r = r_b(s)$ , and  $\varepsilon$  is the unnormalized rms emittance associated with the random motion of the electrons. If there is no magnetic field at the cathode, then  $\langle \hat{P}_q \rangle = 0$ . Any residual magnetic field at the cathode will lead to  $\langle \hat{P}_q \rangle \neq 0$ .

We analyze the beam envelope for equilibrium beam transport in the SLAC 50 MW, 11.4 GHz PPM focusing klystron experiment [10]. The system parameters of the experiment are shown in Table 1. To examine the influence of small residual magnetic field on the beam transport, we analyze two different cases shown in Table 2. In Case I, we assume no residual magnetic field at the cathode, such

that  $\mathbf{g}_b \mathbf{b}_b m c \langle \hat{P}_q \rangle = 0$ . In Case II, however, a residual field of 6.86 G is assumed, corresponding to a beam with a finite canonical angular momentum given by  $\mathbf{g}_b \mathbf{b}_b m c \langle \hat{P}_q \rangle = 4.5 \times 10^{-26}$  Kgm<sup>2</sup>/s. The following dimensionless parameters are derived from Table 2:  $S^2 \mathbf{k}_z(s) = [1.04 \times \sin(2ps/S)]^2$  (with  $S = 2.1$  cm),  $\mathbf{s}_0 = 42.3^\circ = 0.738$ ,  $SK/4\mathbf{s}_0 \mathbf{e} = 10.1$ , and  $\langle \hat{P}_q \rangle / 4\mathbf{e} = 0.0$  in Case I and  $\langle \hat{P}_q \rangle / 4\mathbf{e} = 6.93$  in Case II.

Figure 1 shows plots of the axial magnetic field  $B_z(s)$  and outermost beam radius  $r_b(s)$  versus the propagation distance  $s$  for Cases I and II. In both cases, the amplitude of well-matched (equilibrium) envelope oscillations about the average beam radius is only about 0.005 mm, as seen in Figs. 1(b) and 1(c).

## B. Self-Consistent Simulation of Equilibrium Beam Transport

Self-consistent simulations based on the model described in Sec. II are performed to further investigate the equilibrium beam transport. In the simulations, 4096 macroparticles are used. The macroparticles are loaded according to the rigid-rotor Vlasov distribution [12] with an initial beam radius equal to the equilibrium (matched) beam radius at  $s = 0$  [see Figs. 1(b) and 1(c) for Cases I and II, respectively].

Figure 2 shows, respectively, the initial and final phase-space distributions at  $s = 0.0$  cm and  $s = 42.0$  cm for Case I. Comparing the phase-space plots shown in Figs. 2(e) and 2(f) with the initial phase-space plots in Figs. 2(b) and 2(c), we find an increase in the emittance (randomness) in the transverse electron momentum. The emittance growth is a result of numerical noise in the simulation. However, since the beam dynamics is mostly dictated by space-charge forces for the parameter regime considered here, the emittance growth has little effect on the beam transport properties. In fact, the distribution in the configuration space shown in Fig. 2(d) agrees very well with the initial distribution shown in Fig. 2(a). Moreover, the effective beam radius obtained from the simulation agrees with that obtained from Eq. (8) within 0.2%. In the simulation, no beam loss is detected.

Figure 3 shows, respectively, the initial and final phase-space distributions at  $s = 0.0$  cm and  $s = 42.0$  cm for Case II. The final distributions shown in Figs. 3(d), 3(e), and 3(f) agree very well with

the initial distributions shown in Figs. 3(a), 3(b), and 3(c). In this case, the effects of numerical-noise-induced emittance growth are less pronounced than in Case I (Fig. 2) because the momentum distribution is primarily determined by the finite angular momentum but not by thermal effects. The effective beam radius agrees with Eq. (8) within 0.5%, and no beam loss is detected in the simulation.

### C. Phase Space Structure

It is known that the phase space structure for a matched intense beam in a periodic focusing system exhibits nonlinear resonances and chaotic behavior [14]. To determine how sensitive the equilibrium beam transport is against small perturbations for the parameter region of interest, we examine test-particle dynamics subject to the field configuration consisting of the applied focusing field and the equilibrium self-electric and self-magnetic fields. We make use of the Poincaré surface-of-section method to analyze the phase-space structure of test particles. The results are shown in Fig. 4(a) for Case I with  $\hat{P}_q / 4e = 0$ , and in Fig. 4(b) for Case II with  $\hat{P}_q / 4e = -0.99$ . In Fig. 4, the successive intersections of 15 test-particle trajectories with the phase space  $(r, P_r)$  are plotted every period of the focusing field for 1000 periods. One test particle is initialized at the phase-space boundary of the equilibrium distribution, and the corresponding test-particle orbit is represented by the inner curved arc in Fig. 4(a) and by the innermost contour in Fig. 4(b). The remaining test particles are initialized outside the beam. For both cases shown in Fig. 4, the values of  $\hat{P}_q$  are chosen such that the boundary of the equilibrium distribution extends to  $r = r_b$ . Although the space-charge force outside the beam is nonlinear, the phase space is almost entirely regular. The same results showing regularity in phase space structure are obtained for different values of  $\hat{P}_q$  for Cases I and II.

To summarize the results of this section briefly, we find from self-consistent simulations and detailed phase space analysis that in the absence of RF signal, the equilibrium beam transport in the PPM focusing klystron is robust and no beam loss is expected. These results are in good agreement with the experimental observation [10] of 99.9% beam transmission in the absence of RF signal.

## IV. HALOS INDUCED BY MISMATCHED ENVELOPE OSCILLATIONS



Microwave generation in a klystron is due to the coupling of large-amplitude charge-density and current oscillations in the electron beam with the output RF cavity. The charge-density and current oscillations result from the beating of the fast- and slow-space-charge waves on the electron beam, and are primarily longitudinal. From the point of view of beam transport, the charge-density and current oscillations perturb the equilibrium beam envelope discussed in Sec. III. Although a quantitative understanding of the effects of such large-amplitude charge-density and current oscillations on the dynamics of the electron beam is not available at present, especially in the transverse direction, a qualitative study of such effects is presented in this section. In the present analysis, use is made of the standard one-dimensional cold-fluid model to estimate the amplitude of the envelope mismatch induced by longitudinal current oscillations, and the two-dimensional electrostatic model described in Sec. II is used to explore the process of electron beam halo formation in the transverse phase space of the electron beam.

### A. Estimation of the Mismatch Amplitude

It follows from the linearized continuity equation that the current perturbation  $(\delta I_b)_{f,s}$  is related to the axial velocity perturbation  $c(\delta\beta_b)_{f,s}$  by [15,16]

$$\frac{(\delta I_b)_{f,s}}{I_b} \cong -\frac{\omega}{\omega - \beta_b c k_{f,s}} \frac{(\delta\beta_b)_{f,s}}{\beta_b}, \quad (9)$$

where subscripts  $f$  and  $s$  denotes the fast- and slow-space-charge waves, respectively, and  $\omega$  and  $k_{f,s}$  are the frequency and wave numbers of the perturbations, respectively. Making the long-wavelength approximation for a thin beam, it can be shown that the dispersion relations for the fast- and slow-space-charge waves can be expressed as [15]

$$\omega - \beta_b c k_{f,s} = \pm \frac{\sqrt{\epsilon_{sc}}}{\gamma_b \beta_b^2} \omega, \quad (10)$$

where  $k_f$  assumes plus sign, and  $k_s$  assumes minus sign. In Eq. (10),  $\epsilon_{sc}$  is the longitudinal space-charge coupling parameter. The effective value of  $\epsilon_{sc}$  is estimated to be  $\epsilon_{sc} = 0.012$  for the SLAC PPM focusing klystron [10]. In the klystron, the total current oscillations are the sum of fast- and slow-

space-charge waves with a phase difference of  $\sim 180^\circ$ . As a result, the total current oscillations and the total velocity oscillations are out of phase by  $\sim 180^\circ$ . Therefore, the amplitude of the total current oscillations is given by

$$\frac{(\delta I_b)_{total}}{I_n} \cong -\frac{2\gamma_b \beta_b^2}{\sqrt{\epsilon_{sc}}} \frac{(\delta \beta_b)_{total}}{\beta_b}. \quad (11)$$

This has the important consequence that the perveance of the electron beam varies dramatically along the beam. From the definition of the perveance in Eq. (1), it is readily shown that the amplitude of perveance variation is given by

$$\frac{\delta K}{K} \cong \left(1 + \frac{3\gamma_b \sqrt{\epsilon_{sc}}}{2\beta_b^2}\right) \frac{(\delta I_b)_{total}}{I_b}. \quad (12)$$

For the SLAC PPM focusing klystron [10], Eq. (12) yields  $\delta K / K = 1.45 \times (\delta I_b)_{total} / I_b$ . At the RF output section,  $\delta K / K$  exceeds unity considerably because  $\delta I_b / I_b \approx 1$ . (Note that the current oscillations in the RF output section are highly nonlinear and the maximum current exceeds  $2I_b$ .) From the beam envelope equation (8), the relative amplitude of beam envelope mismatch is estimated to be  $\delta r_b / r_b = 0.56$ , where  $r_b$  is the equilibrium beam radius and  $\delta I_b / I_b = 1$  is assumed. In the self-consistent simulations presented below, we use  $\delta r_b / r_b = 1.0$  in order to take into account the fact that the instantaneous current exceeds  $2I_b$  during high-power operation of the klystron.

## B. Self-Consistent Simulation of Electron Beam Halo Formation

The process of halo formation in intense electron beams is studied using the two-dimensional self-consistent model described in Sec. II. Results of the simulations are summarized in Figs. 5-10 for Cases I and II. In the simulations, 4096 macroparticles are used, and the macroparticles are loaded according to the rigid-rotor Vlasov distribution [5] with an initial beam radius of  $2r_b(0)$ , where  $r_b(0)$  is the equilibrium beam radius at  $s = 0$  [see Figs. 1(b) and 1(c) for Cases I and II, respectively]. The effect of current oscillation build up in the PPM focusing klystron, which requires three-dimensional modeling, is not included in the present two-dimensional simulation.

We first discuss the results of the self-consistent simulation for Case I. In Fig. 5, the effective beam core radius is plotted as a function of the propagation distance  $s$ . The solid curve is obtained from the self-consistent simulation, and the dotted curve is obtained by numerically solving the envelope equation (8) with the emittance calculated in the self-consistent simulation. As expected, results from the self-consistent simulation and envelope equation are in excellent agreement. Although the core radius oscillations are not exactly periodic due to emittance growth, the core radius oscillates with an approximate period of 11.5 cm, such that the envelope typically executes four periods of oscillations in the entire PPM focusing section of the SLAC PPM focusing klystron which is 42 cm long.

Figure 6 shows the phase-space distributions of the electrons at several axial distances during the fourth period of the beam core radius oscillation for Case I. In contrast to the equilibrium phase-space distribution (Fig. 3), significant halos appear at  $s = 34.7, 37.8, 42.0, 44.1,$  and  $46.2$  cm. In the configuration space plots shown in Figs. 6(a) to 6(e) we observe a large variation in the beam core radius during the mismatched envelope oscillation period. The halo particles reach a maximum radius of  $r_h = 6.4$  mm at  $s = 42.0$  cm, where the beam core radius is a minimum and the traveling-wave RF output section is located. Around 1.5% of the electrons are found in the halo at that axial position. Because the maximum halo radius of  $r_h = 6.4$  mm is greater than the actual beam tunnel radius  $r_T = 4.7625$  mm, these halo electrons are lost to the waveguide wall. Therefore, the simulation results show that there will be 1.5% beam electron loss. In terms of beam power loss, 1.5% beam electron loss in the simulation corresponds to 0.2% beam power loss because the lost electrons have given up 88% of their kinetic energies (or have slowed down by about a factor of 2 in their axial velocities). The simulation results agree qualitatively with 0.8% beam power loss observed in the experiment [10]. The discrepancy between the simulation and experimental measurements may be caused by nonlinearities in the applied magnetic fields which are not included in the present simulation.

As the beam propagates in the focusing field, its distribution rotates clockwise in the  $(x, dx/ds)$  phase space, as shown in Figs. 6(f) to 6(j). The particles are initially dragged into the halo at the edges of the phase space distribution, where a chaotic region is formed around an unstable periodic orbit that is located just outside the beam distribution [17]. The unstable periodic orbit is a result of a resonance between the mismatched core envelope oscillations and the particles dynamics. As the halo particles

move away from the beam core, the influence of space charge forces decreases and these halo particles start rotating faster than the core particles, creating the S-shaped distributions observed in Figs. 6(f) to 6(j).

The halo formation is also observed in the  $(x, dy/ds)$  phase space distributions shown in Figs. 6(k) to 6(o). Although the macroscopic (average) canonical angular momentum  $\langle \hat{P}_q \rangle$  is constant in the simulation, the distributions presented in Figs. 6(k) to 6(o) indicate that the distribution of single particle canonical angular momenta induces spread in the  $(x, dy/ds)$  phase space.

Shown in Fig. 7 are the halo radius, i.e., the maximum radius achieved by all of the macroparticles in the self-consistent simulation, and the effective beam core radius as a function of the propagation distance for Case I. It is apparent in Fig. 7 that the halo formation process takes place essentially during the first 4 periods of the envelope oscillations. After reaching  $r_h = 6.4$  mm at  $s = 42.0$  cm, the halo radius saturates. It is interesting to note that once the halo is developed, the halo radius and core envelope radius oscillate in opposite phase, with the former being maximum when the latter is minimum [as seen in Fig. 6(c)] and vice versa.

Second, we discuss the self-consistent simulation results for Case II and the role of small residual magnetic field at the cathode in the halo formation process. Figure 8 shows a plot of the effective beam core radius as a function of the propagation distance  $s$ . In Fig. 8, an excellent agreement is found between the envelope obtained from the self-consistent simulation (solid curve) and the envelope obtained by numerically solving the envelope equation (8) with the emittance calculated in the self-consistent simulation (dotted curve). One of the effects of the residual magnetic field at the cathode is to decrease the period of the envelope oscillations. The period for case II is 10.5 cm, slightly shorter than the period found in Case I (Fig. 5). The envelope executes four periods of oscillations in the entire PPM focusing section of the SLAC klystron.

Figure 9 shows the phase-space distributions of the electrons at several axial distances during the fourth period of the beam core radius oscillations for Case II. The configuration space distributions shown in Figs. 9(a) to 9(e) do not exhibit sizable halos. In particular, comparing Figs. 9(a)-9(e) with the configuration space distributions for Case I, shown in Figs. 6(a)-6(e), it is clear that the halos are much more pronounced in Case I. Analyzing Figs. 9(d) and 9(e) in more detail we observe hollow regions in

the interior of the beam and that the existing halos appear in the form of vortices. Because the beam rotation period is calculated to be approximately 3 times the envelope oscillation period, the hollow regions and associated vortex structure might be a result of a diocotron instability process driven by a resonance between the envelope oscillations and the beam rotation.

The properties of the phase space distributions shown in Figs. 9(f) to 9(o) resemble the properties discussed in Case I with regard to the rotation in the  $(x, dx/ds)$  phase space and the spread in the  $(x, dy/ds)$  phase space. In comparison with Case I, the main difference is that the phase space distributions in Case II exhibit vortex structures.

Figure 10 shows the halo radius and effective beam core radius as a function of the propagation distance for Case II. Although sizable halos arise in the simulation after many periods of envelope oscillations, it is evident that the halo formation process is slower in Case II than in Case I (see Fig. 7). In particular, despite that the initial beam radius in Case II is larger than in Case I, the halo radius in Case I is greater than that in Case II at the output section ( $s = 42$  cm) of the PPM focusing klystron. Because the halo radius at  $s = 40$  cm is 5.3 mm and is still greater than the beam tunnel radius, the electrons in the halo are lost to the waveguide wall. Nevertheless, these results indicate that a small residual magnetic field at the cathode plays an important role in delaying the halo formation process and might be used to prevent electron beam loss in future experiments.

## V. CONCLUSIONS

We have studied equilibrium beam transport in a periodic magnetic focusing field in the absence of RF signal, and the behavior of a high-intensity electron beam under a current-oscillation-induced mismatch between the beam and the magnetic focusing field. Detailed simulation results were presented for choices of system parameters corresponding to the 50 MW, 11.4 GHz periodic permanent magnetic (PPM) focusing klystron experiment performed at the Stanford Linear Accelerator Center (SLAC).

From self-consistent simulations and detailed phase space analysis, we found that in the absence of RF signal, the equilibrium beam transport is robust, and that there is no beam loss, which is in agreement with experimental measurements. During the high-power operation of the klystron, however, we found that the current-oscillation-induced mismatch between the beam and the magnetic focusing field

produces large amplitude envelope oscillations. We estimated the amplitude of envelope oscillations using a one-dimensional cold-fluid model. From self-consistent simulations we found that for a mismatch amplitude equal to the beam equilibrium radius, the halo reaches 0.64 cm in size and contains about 1.5% of total beam electrons at the RF output section for a beam generated with a zero magnetic field at the cathode. Because the halo radius is greater than the actual beam tunnel radius, these halo electrons are lost to the waveguide wall, yielding 0.2% beam power loss. The simulation results agree qualitatively with 0.8% beam power loss observed in the experiment [10]. The discrepancy between the simulation and experimental measurements may be caused by nonlinearities in the applied magnetic fields which are not included the present simulation.

We also studied the influence of a small residual magnetic field at the cathode on the equilibrium beam transport and electron beam halo formation during high-power operation of the klystron. We found that the equilibrium beam radius increases with the residual magnetic field. Although the halo grows in size to reach the waveguide wall the RF output section and a nonlinear vortex structure develops in the electron beam, we found that the onset of halo formation is delayed, which might be used to prevent electron beam loss in future experiments.

Although the results presented in this paper are based on a two-dimensional electrostatic model, they give a good qualitative description of the process of halo formation in high-power PPM focusing klystron amplifiers and suggest that halo formation is a potential mechanism for electron beam losses in such devices.

## **ACKNOWLEDGMENTS**

This work was supported by the Air Force Office of Scientific Research, Grant No. F49620-97-1-0325, and in part by the Department of Energy, Office of High Energy and Nuclear Physics, Grant No. DE-FG02-95ER-40919.

## REFERENCES

1. See, for example, *Special Issue on High-Power Microwave Generation*, edited by E. Schamiloglu and Y. Y. Lau, IEEE Trans. Plasma Sci., vol. 26, No. 3, June, 1998.
2. F. J. Agee, "Evolution of pulse shortening research in narrow band, high-power microwave sources," IEEE Trans. Plasma Sci., vol. 26, No. 3, pp. 235-245, 1998.
3. J. Benford and G. Benford, "Pulse shortening in high-power microwave sources," Proceedings of the 11th International Conference on High-Power Particle Beams, Institute of Plasma Physics, Academy of Science of the Czech Republic, 1996, p. 217.
4. K. J. Hendricks, P. D. Coleman, R. W. Lemke, M. J. Arman, and L. Bowers, "Extraction of 1 GW of rf power from an injection locked relativistic klystron oscillator," Phys. Rev. Lett., vol. 76, No. 1, pp. 154-157, Jan., 1996; and references therein.
5. M. D. Haworth, G. Baca, J. N. Benford, T. Englert, K. Hackett, K. J. Hendricks, D. Henley, M. LaCour, R. W. Lemke, D. Price, D. Ralph, M. Sena, D. Shiffler, and T. A. Spencer, "Significant pulse-lengthening in a multigigawatt magnetically insulated transmission line oscillator," IEEE Trans. Plasma Sci., vol. 26, No. 3, pp. 312-319, 1998.
6. F. Hegeler, C. Grabowski, and E. Schamiloglu, "Electron density measurements during microwave generation in a high-power backward-wave oscillator," IEEE Trans. Plasma Sci., vol. 26, No. 3, pp. 275-281, June, 1998.
7. D. Price, J. S. Levine, and J. N. Benford, "Diode plasma effects on the microwave pulse length from relativistic magnetrons," in *Intense Microwave Pulses V*, edited by H. E. Brandt, Proc. SPIE, vol. 3158, 1997, p. 13.
8. C. Chen and R. A. Jameson, "Self-consistent simulation studies of periodically focused intense charged-particle beams," Phys. Rev. E, vol. 52, No. 3, pp. 3074-3080, Sept., 1995.
9. Y. Fink, C. Chen, and W. P. Marable, "Halo formation and chaos in root-mean-square matched beams propagating through a periodic solenoidal focusing channel," Phys. Rev. E, vol. 55, No. 6, pp. 7557-7564, June, 1997.



10. D. Sprehn, G. Caryotakis, E. Jongewaard, and R. M. Phillips, "Periodic permanent magnetic development for linear collider X-band klystrons," Proc. XIX International Linac Conf., Argonne National Laboratory Report ANL-98/28, 1998, p. 689.
11. M. Hess, R. Pakter, and C. Chen, "Green's function description of space charge in intense charged-particle beams," Proceedings of 1999 Particle Accelerator Conference, 1999, p. 2752.
12. C. Chen, R. Pakter, and R. C. Davidson, "Rigid-rotor Vlasov Equilibrium for an intense charged-particle beam propagating through a periodic solenoidal magnetic field," Phys. Rev. Lett., vol. 79, No. 2, pp. 225-228, July, 1997.
13. R. C. Davidson and C. Chen, "Kinetic description of high-intensity beam propagation through a periodic focusing field based on the nonlinear Vlasov-Maxwell equations," Part. Accel., vol. 59, pp. 175-250, 1998.
14. C. Chen, R. Pakter, and R. C. Davidson, "Phase space structure for matched intense charged-particle beams in periodic focusing transport systems," Phys. Plasmas, vol. 6, No. 9, pp. 3674-3657, 1999.
15. C. Chen, G. Bekefi, and P. Catravas, "Growth and saturation of simulated beam modulation in a two-stream relativistic klystron amplifier," Appl. Phys. Lett., vol. 62, No. 14, pp. 1579-1581, April, 1993.
16. M. Friedman, J. Krall, Y. Y. Lau, and V. Serlin, "Efficient generation of multigigawatt rf power by a klystronlike amplifier," Rev. Sci. Instrum., vol. 61, No. 1, pp. 171-181, Jan., 1990.
17. R. L. Gluckstern, "Analytic model for halo formation in high-current ion linacs," Phys. Rev. Lett., vol. 72, No. 9, pp. 1247-1250, August, 1994.

Table 1. SLAC 50 MW, 11.4 GHz, PPM Focusing Klystron Experiment

Beam Current $I_b$	190 A
Beam Voltage	464 kV
Cathode Radius	2.86 cm
Cathode Temperature $T_b$	800° C †
Beam Radius	2.38 mm†
Pipe Radius	4.7625 mm
Total Tube Length	90.0 cm
Focusing Field Period Length	2.1 cm
PPM Focusing Section Length	42.0 cm
RMS Axial Magnetic Field	1.95 kG

† estimated

Table 2. System Parameters Used in the Simulation

BASIC PARAMETER	CASE I	CASE II
Beam Current $I_b$	190 A	190 A
Beam Voltage	464 kV	464 kV
Cathode Radius	2.86 cm	2.86 cm
Residual Magnetic Field at Cathode	0.0 G	6.86 G
Cathode Temperature $T_b$	800° C	800° C
Beam Radius	2.05 mm	2.38 mm
Pipe Radius	9.0 mm	9.0 mm
Total Tube Length	90.0 cm	90.0 cm
Focusing Field Period Length	2.1 cm	2.1 cm
PPM Focusing Section Length	42.0 cm	42.0 cm
RMS Axial Magnetic Field	1.95 kG	1.95 kG

## FIGURE CAPTIONS

Figure 1. Plots of the axial magnetic field in (a) and outermost beam radius  $r_b(s)$  versus the propagation distance  $s$  for equilibrium beam propagation corresponding to Case I in (b) and Case II in (c). The dimensionless parameters are:  $S^2 \mathbf{k}_z(s) = [1.04 \times \sin(2ps/S)]^2$ ,  $\mathbf{s}_0 = 42.3^\circ = 0.738$ ,  $SK/4\mathbf{s}_0 \mathbf{e} = 10.1$ , and  $\langle \hat{P}_q \rangle / 4\mathbf{e} = 0.0$  in (b) and  $\langle \hat{P}_q \rangle / 4\mathbf{e} = 6.93$  in (c).

Figure 2. Plots of the initial and final particle distributions at  $s = 0.0$  and  $42.0$  cm for the equilibrium beam corresponding to the parameters in Case I.

Figure 3. Plots of the initial and final particle distributions at  $s = 0.0$  and  $42.0$  cm for the equilibrium beam corresponding to the parameters in Case II.

Figure 4. Poincaré surface-of-section plots for 15 test particle trajectories under the influence of the PPM focusing field shown in Fig 1(a) and the self-electric and self-magnetic forces of the equilibrium beams. Shown in (a) is for Case I with single particle canonical angular momentum  $\hat{P}_q = 0$ , and in (b) for Case II with single particle canonical angular momentum  $\hat{P}_q / 4\mathbf{e} = -0.99$ .

Figure 5. Plot of the effective beam core radius  $r_b(s)$  versus the propagation distance  $s$  for mismatched beam propagation corresponding to Case I. The solid curve is obtained from the self-consistent simulation, whereas the dotted curve is obtained by numerically solving the envelope equation (8) with the emittance calculated in the self-consistent simulation.

Figure 6. Plots of particle distributions in phase space at  $s = 34.7, 37.8, 42.0, 44.1,$  and  $46.2$  cm for Case I.

Figure 7. Plots of the halo radius (solid curve) and core radius (dashed curve) as a function of the propagation distance  $s$  for Case I.

Figure 8. Plot of the effective beam core radius  $r_b(s)$  versus the propagation distance  $s$  for mismatched beam propagation corresponding to Case II. The solid curve is obtained from the self-consistent simulation, whereas the dotted curve is obtained by numerically solving the envelope equation (8) with the emittance calculated in the self-consistent simulation.

Figure 9. Plots of particle distributions in phase space at  $s = 31.5, 33.6, 36.8, 39.9,$  and  $42.0$  cm for Case II.

Figure 10. Plots of the halo radius (solid curve) and core radius (dashed curve) as a function of the propagation distance  $s$  for Case II.

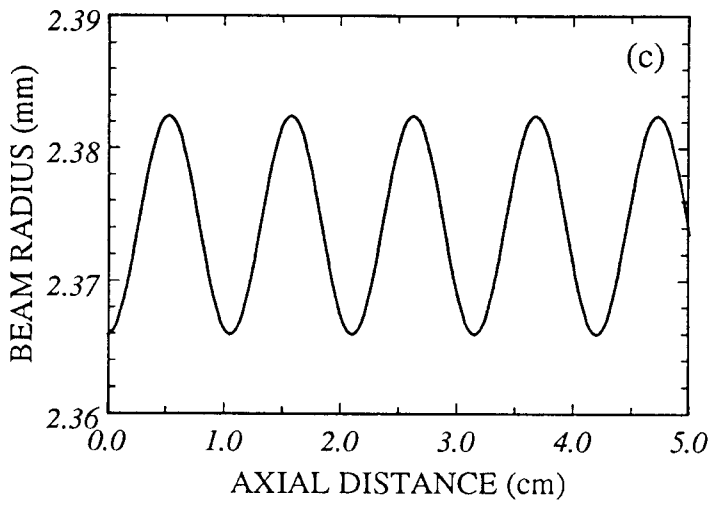
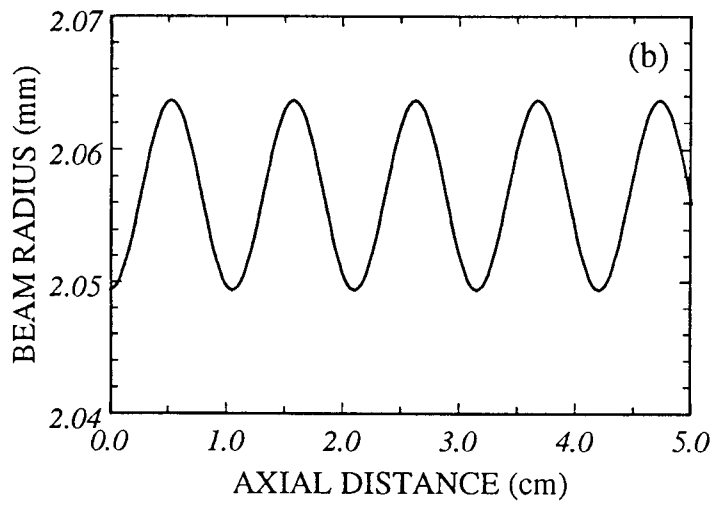
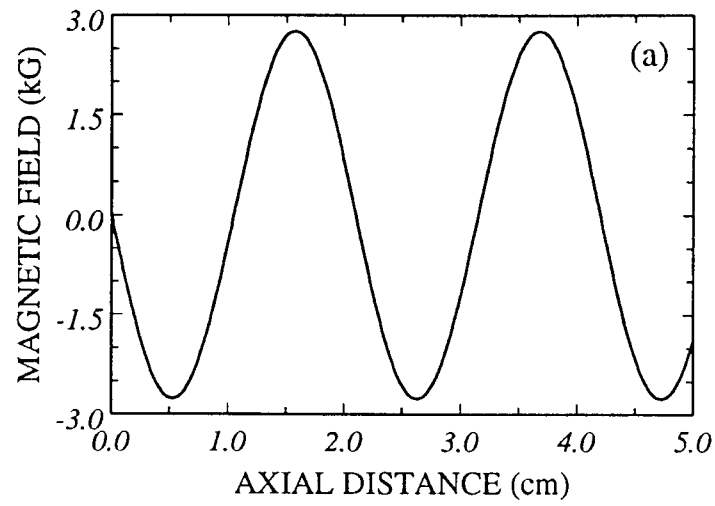


Fig. 1

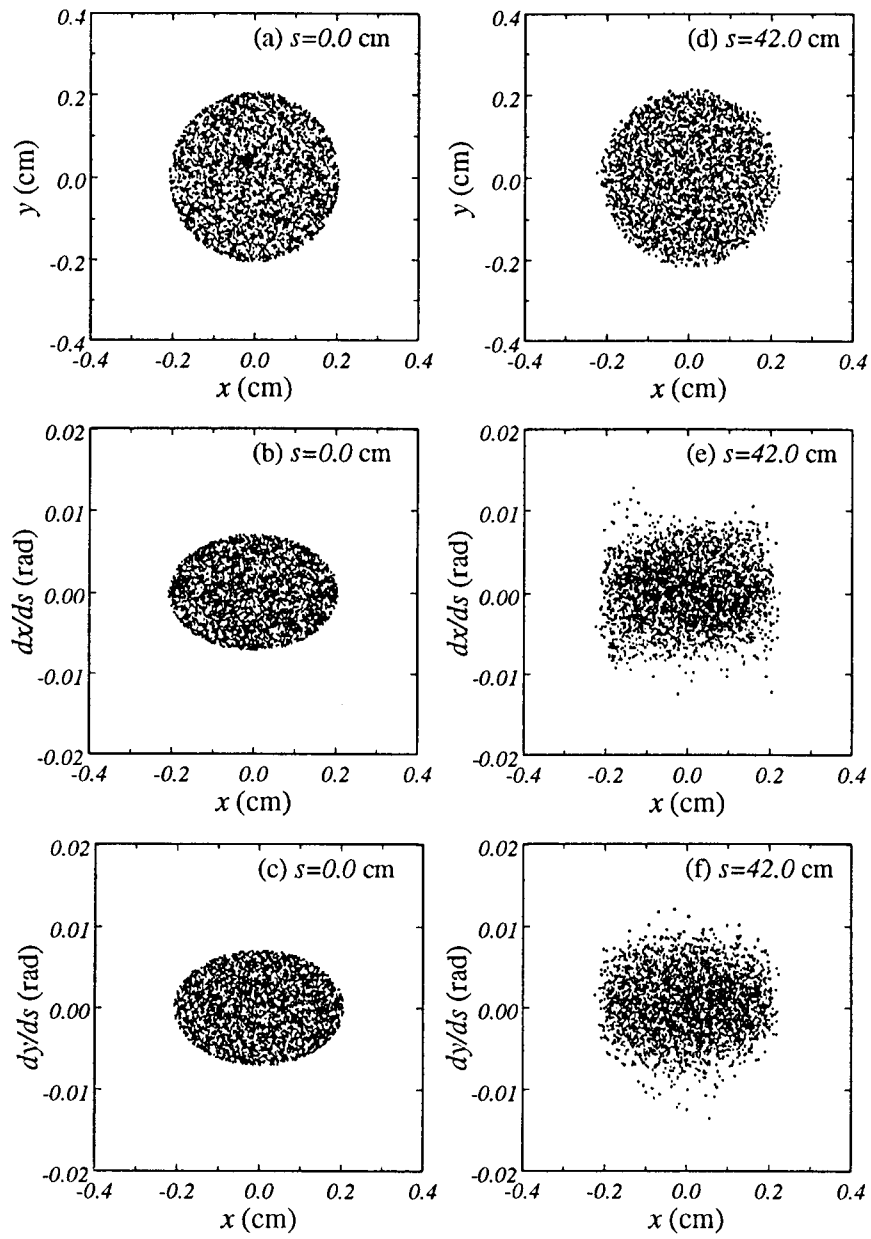


Fig. 2

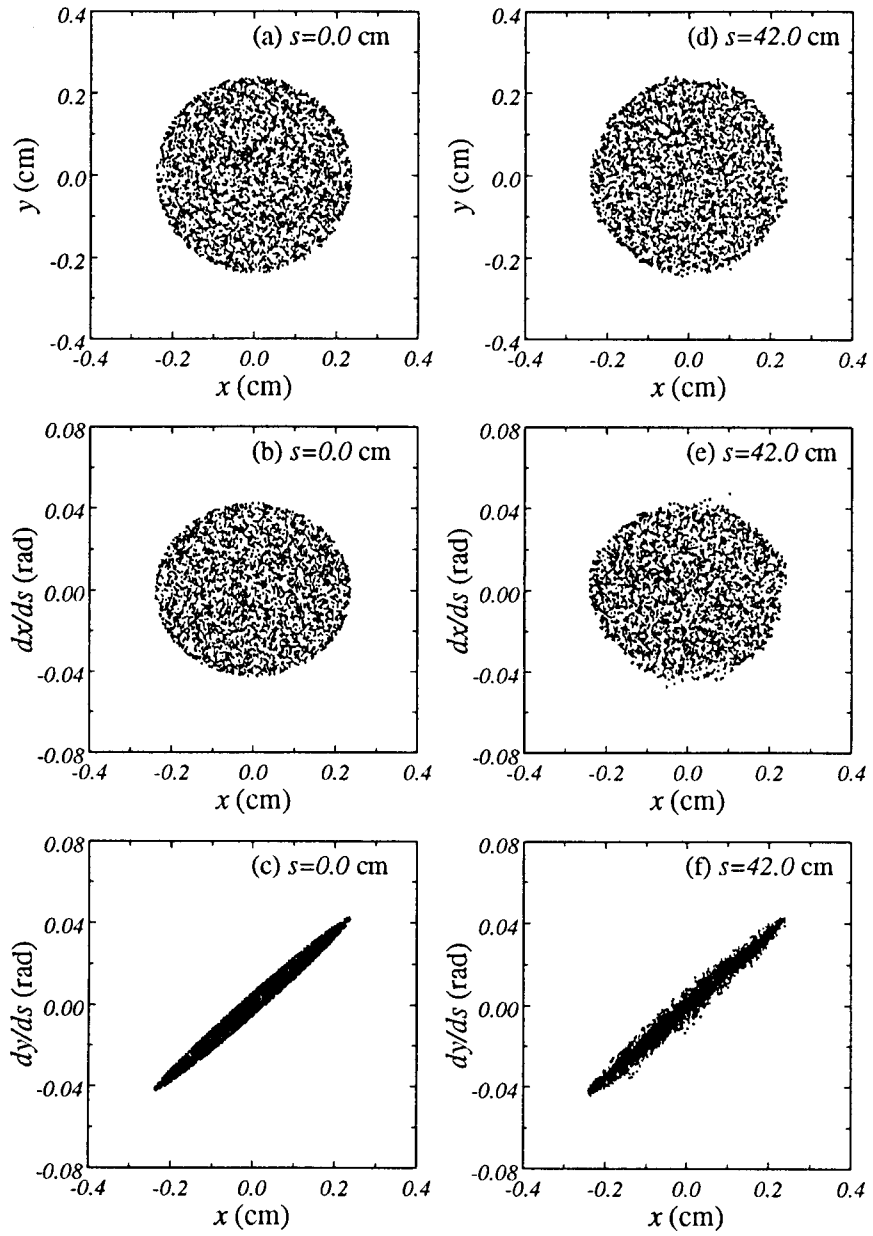


Fig. 3

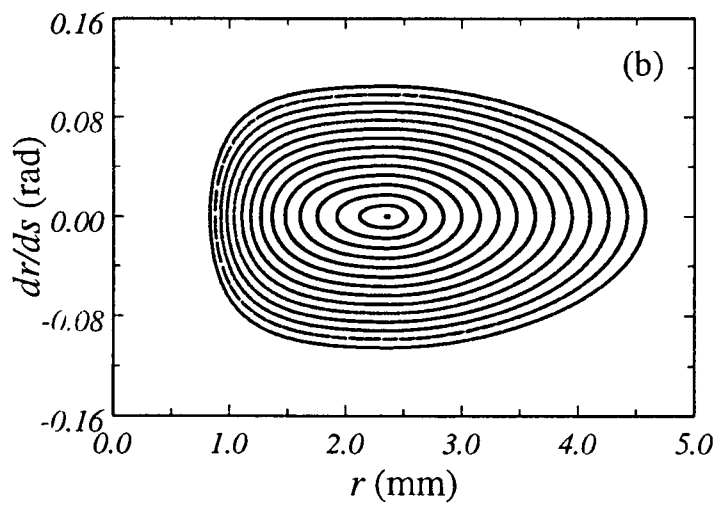
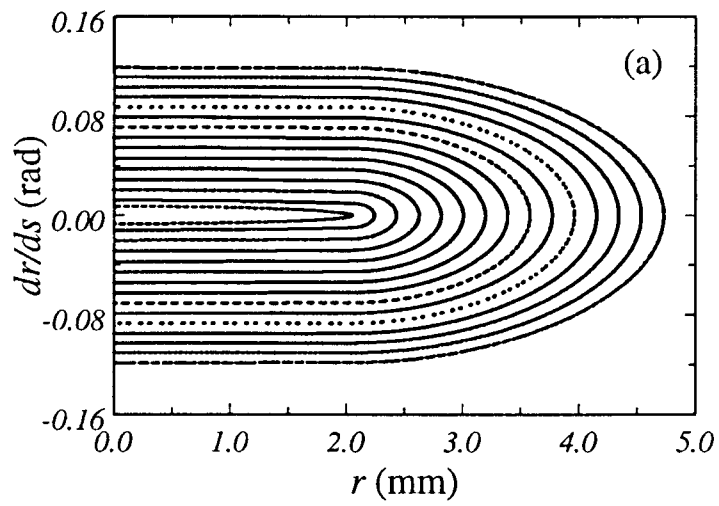


Fig. 4



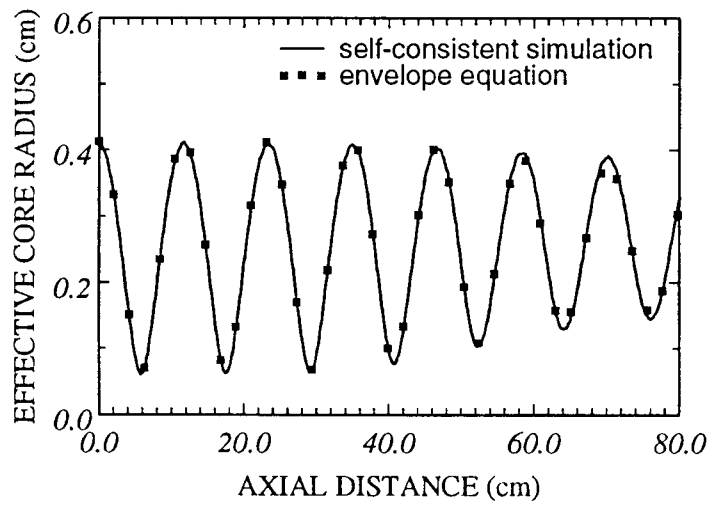


Fig. 5

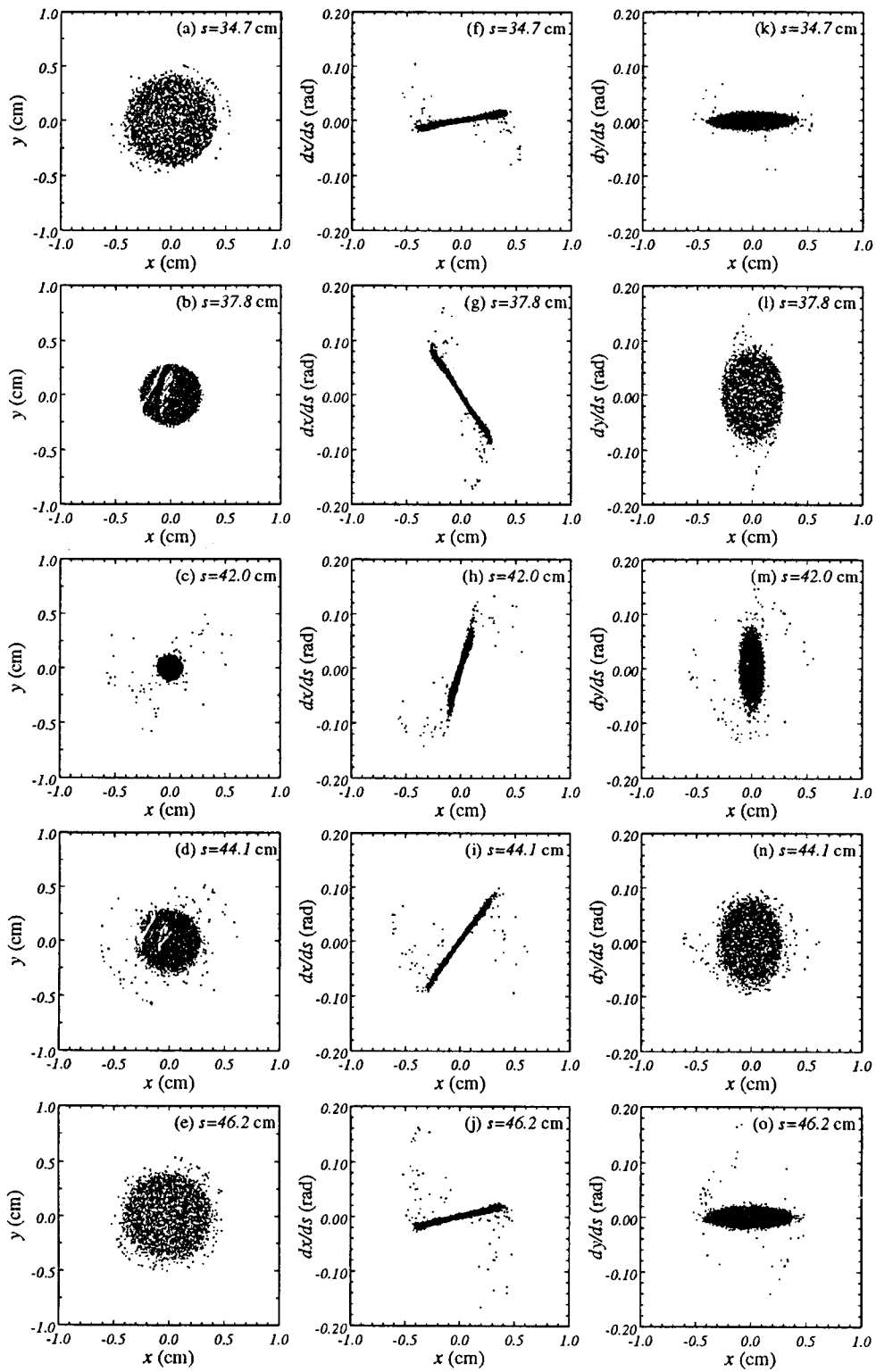


Fig. 6

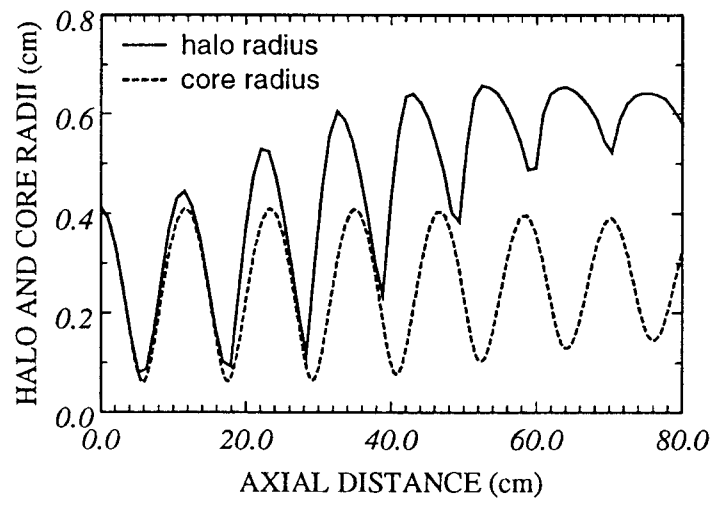


Fig. 7

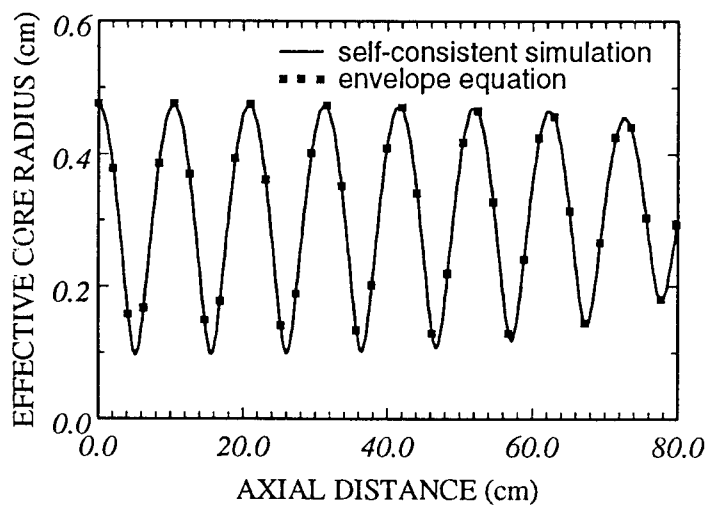


Fig. 8

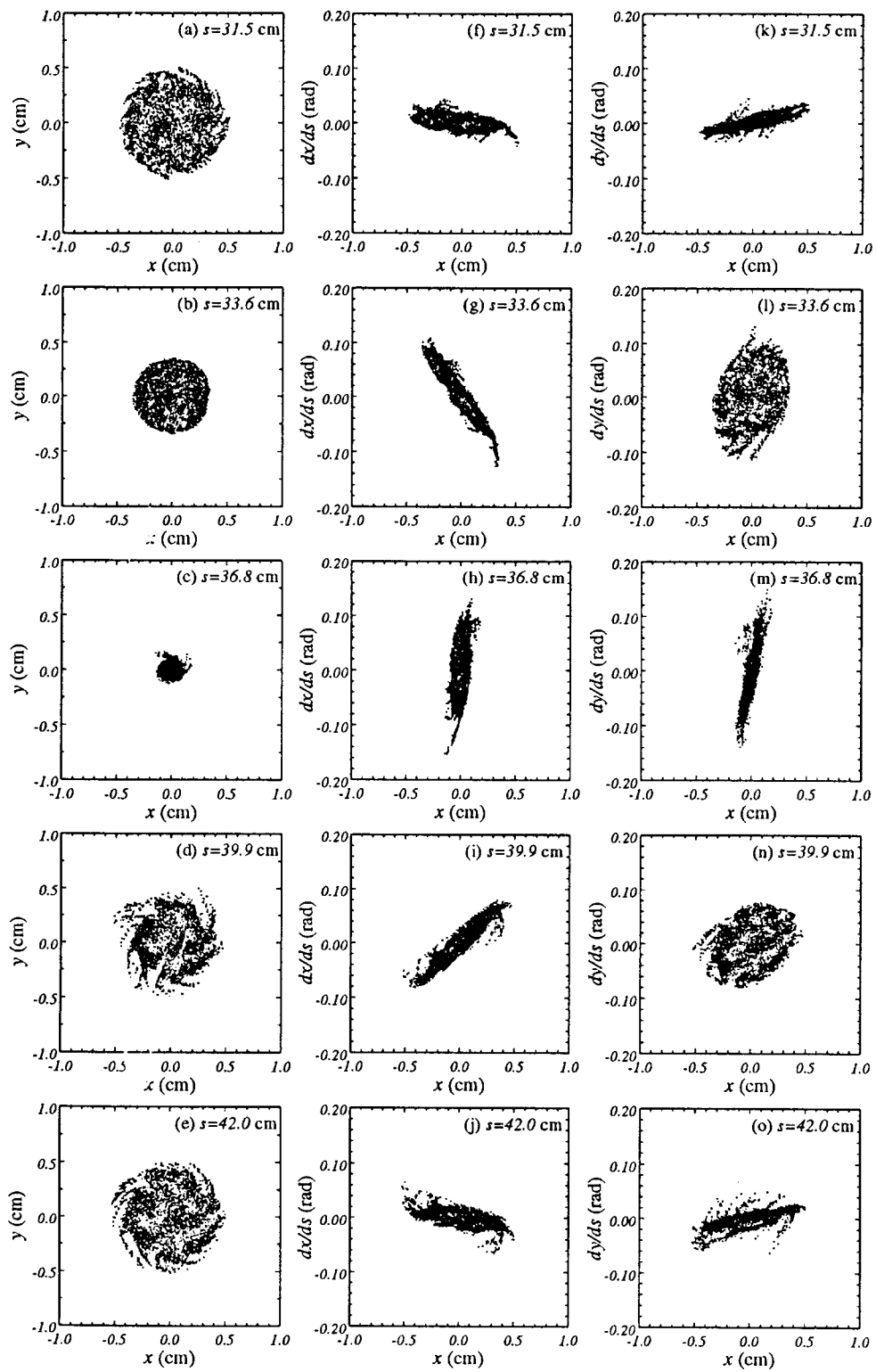


Fig. 9

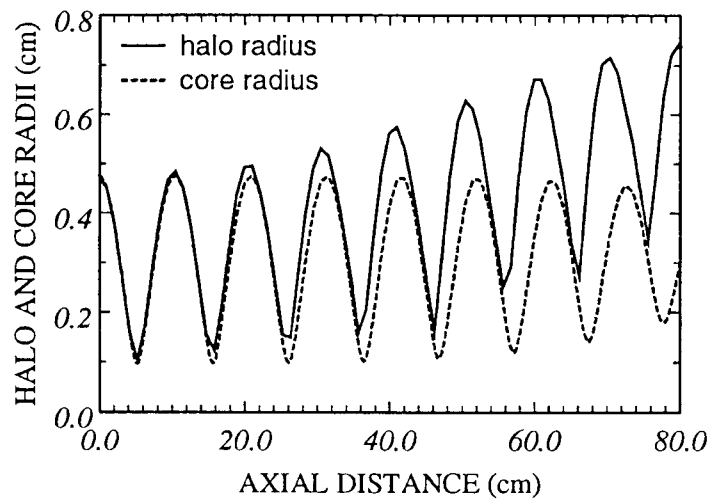


Fig. 10